Development of photocatalytic nanostructured TiO_2 and NiO/TiO_2 coatings by DC magnetron sputtering for photocatalytic applications

Antía Villamayor[a*], Thomas Pomone[b], Eva G-Berasategui[a], Peter Kelly[b], Sergio Perero[c], Victoria Laura Barrio[d], Monica Ferraris[c]

[a]TEKNIKER, Parke Teknologikoa, Calle Iñaki Goenaga 5, 20600, Eibar Gipuzkoa, Spain

[b]Surface Engineering Group, Manchester Metropolitan University, Manchester M1 5GD, UK

[c]Politecnico di Torino, DISAT - Department of Applied Science and Technology, corso Duca degli Abruzzi 24, I-10129, Torino, Italy

[d]Dept. of Chemical and Environmental Engineering, Faculty of Engineering, University of the Basque Country (UPV/EHU), Plaza Ingeniero Torres Quevedo, 1, 48013 Bilbao, Spain

Abstract

High photocatalytic activity layers were obtained by combining a TiO_2 nanostructured coating support with 10 nm and 20 nm NiO layers synthesized by direct current (DC) magnetron sputtering. In order to improve the TiO_2 crystallinity several sputtering process parameters were studied. The TiO_2 and NiO/TiO_2 coatings were characterized through XPS, XRD, FESEM, AFM

* Corresponding author: Antía Villamayor Tel.: +3466213849;

TEKNIKER, Parke Teknologikoa, Calle Iñaki Goenaga 5, 20600, Eibar Gipuzkoa, Spain

*E-mail address: antia.villama*yor@tekniker,es

and UV transmittance measurements, in the latter case, for band gap determination. The photocatalytic activity of the coatings was tested through methylene blue degradation under UV light. The formation of a p-n heterojunction between the TiO_2 and NiO layers improved the degradation rates, compared to the bare TiO_2 layers; however, almost no difference can be seen when increasing the NiO sputtering power and subsequently the coating thickness to higher values than 20 nm.

Keywords: DC magnetron sputtering, Photocatalytic coatings, p-n heterojunctions, NiO catalyst.

---

1. Introduction

Recently, the rise of the "fast fashion" industry has sparked profound concern, as it worsens the damaging effects of the textile industry on the environment [1]. Thus, it has become critical to find efficient and non-polluting wastewater cleaning methods that allow the removal of toxic organic dyes.

Photocatalysis has drawn attention for wastewater treatment, as a light-driven, cost-effective and sustainable method that can easily degrade organic pollutants. Among photocatalytic compounds, crystalline titanium oxide [2], specifically the anatase phase, is widely known for its use as an organic pollutant oxidant in wastewater treatment [3–5], but also for hydrogen production [6–8], or to be incorporated in biological materials [9]. When a photon, with equal or higher energy than the band gap of anatase TiO_2 (3.2 eV), irradiates the TiO_2 conduction band (CB), electron-hole pairs are generated. These charge carriers diffuse all over the surface, reacting with surrounding compounds, forming radicals ($^{\cdot}OH$, $^{\cdot}O_2$) able to carry out oxidation reactions that mineralize organic molecules [10]. Moreover, its low toxicity, low cost, and high stability are beneficial for the aforementioned applications. Nevertheless, the photoactivity of TiO_2 is hindered by the high recombination rate of the electron-hole pairs, reducing the efficiency of this

material to carry out photocatalytic reactions. Several strategies can be followed to improve TiO_2 photoactivity such as metal doping [11,12], the formation of p-n heterojunctions [13–15] or surface modification [16]. The formation of a p-n heterojunction with an n-type semiconductor appears to be an efficient approach to overcoming obstacles such as high recombination rates and low charge carrier transfer. When a p-n heterojunction is formed, the excited electrons migrate from the n-type semiconductor to the p-type one, which has a lower energy conduction band (CB); meanwhile, the holes move from the p-type to the n-type valence band (VB). The excitons' movement creates a built-in electric field with a negative charge at the interface of both semiconductors, facilitating charge separation and diminishing the recombination rate, resulting in an improvement of the photocatalytic performance [17] (Figure 1). TiO_2 can be combined with several semiconductors such as Fe_2O_3 [18], SnO_2 [19], ZnO [20] or NiO [21] to achieve lower recombination rates, although recently, NiO has received more attention, due to its improved charge separation and cost-effectiveness [22]. As a p-type semiconductor, NiO has remarkable optoelectronic properties, which translates into improved charge carrier separation, higher hole mobility and promoting interfacial charge transfer [23,24]. Besides, the polar surface of NiO seems to improve the adsorption of several organic compounds and

dyes [21,25–28]. The combination of all these features makes this material suitable for numerous applications such as hydrogen production[29], electrochromic devices [30] or sensors [31].

For catalyst development, wet-chemical methods such as sol-gel techniques are commonly preferred because they can lead to higher specific surface areas, a fundamental factor in achieving good photocatalytic activity [32,33]. However, these methods not only produce catalysts with low homogeneity, durability and highly toxic by-products, but they are also unsuitable for industrial upscaling, which is fundamental for large scale production of large-area thin films. Furthermore, as the catalyst is not fixed onto a substrate, the method requires a post-filtration treatment, which could be detrimental to the environment [34]. Physical vapor deposition (PVD) technologies, in particular magnetron sputtering, could resolve the aforementioned drawbacks, arising as a promising alternative to chemical methods, especially in terms of industrial upscaling. Magnetron sputtering allows the manufacture of large-area catalytic thin films immobilized onto a substrate and with excellent physical properties such as high adhesion or durability. The production of photocatalytic TiO_2 films by means of magnetron sputtering has been already widely explored for several applications including wastewater treatment [35–41]. Regarding the use of magnetron sputtering to

develop photocatalytic TiO_2 p-n heterojunctions, several combinations have been investigated, including WO_3/TiO_2 [42], CuO/TiO_2 [43] or ZnO/TiO_2 [44], however, as far as our knowledge is concerned, there are only a few examples of sputtered NiO/TiO_2. Thus, a NiO/TiO_2 transparent photovoltaic cell was developed through magnetron sputtering, with the TiO_2 acting as a UV light detector and NiO as the visible light absorber [45]. Elsewhere, a NiO layer was sputtered by DC reactive magnetron sputtering over TiO_2 for electrochemical reduction of N_2 to study the "π-back donation" mechanism [46]. Given that PVD methods seem to be unusual for the fabrication of this type of heterojunctions, it is interesting to explore this technology, taking also into account its potential to upscale to an industrial level the fabrication of effective, durable and non-toxic photocatalytic films.

In this work, porous, columnar thin films of TiO_2 and NiO/TiO_2 have been developed by reactive DC magnetron sputtering in an industrial sputtering chamber, to study the effect of NiO on their photocatalytic activity. The aim of this research is to (i) prove that magnetron sputtering is a suitable method for large-scale production of NiO/TiO_2 thin films and (ii) to improve the photocatalytic performance for dye degradation of TiO_2 through the formation of a p-n heterojunction. For that purpose, the study of TiO_2 sputtering process parameters, such as sputtering power and pressure, was

performed, optimizing the TiO_2 film in terms of crystallinity and morphology. Once the desired TiO_2 film was obtained, NiO was deposited on top of TiO_2, resulting in nominally 10 nm and 20 nm thick NiO layers. The photocatalytic activity of both TiO_2 and NiO/TiO_2 coatings has been tested for methylene blue (MB) degradation under UV light.

2. Materials and methods

2.1. Deposition

Glass slides (2,6 x 7,6 cm^2) and monocrystalline silicon (100) wafers were used as substrates. Previous to the deposition, in order to remove any residue or contamination from the samples, glass slides were cleaned with an alkaline solution, rinsed with isopropyl alcohol and dried with hot air. For the Si wafers, only the last two steps were done.

To prevent the migration of Na^+ ions present in glass substrates, 250 nm of SiO_2 was deposited as an initial barrier layer. The SiO_2 deposition was carried out by DC magnetron sputtering in reactive mode in Ar while regulating the O_2 flow at 20% with a Speedflo®TM controller (Gencoa Ltd). The magnetron was driven using an Advanced Energy Pinnacle Plus in pulsed DC mode, applying a sputtering power of 2 kW and a pulse frequency of 75 kHz with a duty cycle of 70% at a pressure of 0,62 Pa.

For the TiO_2 coating deposition process optimization, three pressures and two sputtering power densities were studied. The sputtering parameters described below were selected for the TiO_2 coating application, according to the desired crystallinity and morphology for the coatings.

Titanium dioxide coatings were deposited by DC magnetron sputtering technology in an industrial vacuum chamber (80 x 60 cm^2), designed and manufactured at TEKNIKER, equipped with one unbalanced magnetron connected to an Advanced Energy Pinnacle DC power supply. A titanium target (55 x 12,5 cm^2, 99.99% purity) was used and the substrates were placed on a fixed substrate holder at ground potential, positioned at 5 cm in front of the target. The chamber base pressure was $2x10^{-4}$ Pa and the target was pre-sputtered with Ar for 4 min 0,95 Pa, to remove the oxide layer present on the Ti target. Following this, the deposition of TiO_2 was carried out in reactive mode with a 110/40 sccm ratio of Ar/O_2 gas flow, operating in fully oxidized mode due to the absence of continuous feedback control. This mode is needed because of the high instability of the TiO_2 reactive deposition process in transition mode [47,48]. The sputtering power was set at 4 kW, the working pressure was 8.2 Pa and the substrate was at ground potential. The deposition rate was approximately 0,2 nm/s with a total thickness of around 700 nm. After the deposition process, the samples were post-annealed for 2h at 450ºC.

The deposition of the NiO thin films was performed in a Kenosintec™ sputtering chamber, equipped with three confocal circular magnetron cathodes. DC powers of 25 W or 50 W were applied to a Ni target (diameter 152.4 mm, 99.99% purity) for 10 minutes with an Advanced Energy MDX^{TM} power supply. The base pressure of the chamber was $6.5x10^{-3}$ Pa and a working pressure of 1.1 Pa was maintained during the deposition with a gas flow of 55 sccm of Ar. The distance from the samples to the target was 245 mm. The initial aim was to obtain a Ni metallic coating but NiO was formed, probably due to oxidation after deposition or, maybe due to the presence of some oxygen inside the chamber.

2.2. Characterization Methods

To assess the crystal structure of the thin films produced, X-ray diffraction (XRD) was performed on a Panalytical Xpert^{TM} system. CuKα1 radiation at 0.154 nm was used in grazing incidence mode at 3°, over a scan range from 20 to 80° 2θ. The acceleration voltage and applied current were set at 40 kV and 30 mA, respectively. Morphology and thickness studies were carried out using an ULTRA Plus Carl-Zeiss field emission scanning electron microscope (FESEM) and Solver PRO NT-MDT atomic force microscope (AFM). Raman Spectroscopy was performed with a Raman Renishaw for each sample. The laser used for the acquisition of the spectra operated at a

wavelength of 514 nm with a power of 10 mW. The optical characterization of the coatings deposited on glass was performed using an Ocean Optics USB4000 UV-Vis spectrometer. The oxidation state information of the samples was obtained by X-ray photoelectron spectroscopy (XPS), performed with a SUPRA photoelectron spectrometer (Kratos Analytical Ltd.) equipped with Mg K X-rays as the primary excitation source. The binding energy was referenced to the C 1s line at 284.8 eV for calibration, and a Gaussian function was applied for curve fitting with a Shirley background.

2.3. Photocatalytic activity measurements for methylene blue degradation

The photocatalytic activity of the samples was assessed by methylene blue (MB) degradation tests. Each 2,5x 2,5 cm^2 sample, cut from the original samples, was placed in a quartz cuvette containing 50 mL of methylene blue solution (from Alfa Aesar) with a concentration of 2 $\mu molL^{-1}$. Before testing, the samples were placed in the dark for 1h under continuous stirring to reach the adsorption/desorption equilibrium. The samples were then irradiated for 1h with UV-A sources (15 W Sankyo Denki BB lamps). The main peak of the UV source was measured at 365 nm. An Ocean Optics USB4000 UV-Vis spectrometer was used to monitor the main methylene blue absorption peak (664 nm). Finally, the pseudo-first-order rate constants k_α were obtained for

each sample by plotting $Ln(A_0/A_t)$ against time in order to compare the different photocatalytic activities [49,50].

2.5. Stability measurements

The stability of both NiO/TiO_2 samples was studied by repeating the degradation test of MB as described in Section 2.3. After each measurement, the samples were cleaned with distilled water and dried with compressed air and the operation was repeated with both samples nine more times.

3. Results and discussion

3.1. Characterization

FESEM was used to determine the morphology of the coatings. Figures 2 (a, b) shows the columnar porous structure of the TiO_2 coating, which is similar in appearance to the porous structure described in the Thornton Structure Zone model [51]. The measured thickness of the TiO_2 coating is around 740 nm with column diameters ranging from 60 nm to 160 nm (Figure S3). For the NiO films, only the 20 nm thick film could be measured through FESEM (Figure S2) as the 10 nm layer did not form a continuous film and could not be measured this way. Regarding the morphology of the NiO coatings, the 10 nm NiO (Figure 2 c, d) layer changes subtly the surface of the columns TiO_2, with the appearance of a small cluster-like structure that can be seen on top

of these columns, although no changes are apparent in terms of film porosity. When the thickness is increased from nominally 10 nm to 20 nm the surface morphology changes are much more relevant (Figure 2. e, f). The 20 nm NiO layer forms an almost continuous film over the TiO_2 columns with a cauliflower-like morphology, reducing its porosity remarkably. The reason for film densification could be the change of the sputtering power from 25W to 50W, because not only is the deposition rate increased at higher powers, but the incident sputtered particles arrive at the film surface with higher energy.

The surface and thickness of the NiO films were further analysed by atomic force microscopy (AFM). The thickness of both NiO films was obtained by step height measurements in different regions of the coatings. The average thicknesses of the samples were 23,8 ± 3,6 nm and 8,7 ± 1 nm (Figure S1), respectively. Through AFM analysis, the roughness of the NiO films was also investigated. Average roughness (Ra) values, which correspond to the arithmetic average of the deviations of a height profile compared to a mean line and root-mean-square roughness (Rq), which is the quadratic average of a height profile compared to a mean line were the parameters selected for roughness evaluation. 3D-AFM images of the 10 nm and 20 nm NiO samples, deposited at a sputtering power of 25 W and 50 W, respectively, are depicted

in Figures 3a and 3b. When sputtering power was increased a smoother surface was formed, lowering the roughness of the 20 nm NiO film compared to the 10 nm one, as indicated by the Ra and Rq values of 7,4 nm and 9,4 nm for the 20 nm film, compared with the 10 nm layer Ra and Rq values of 10,2 nm and 12,7 nm (Table S1). These values can be used as a comparison between the NiO films, but not as a quantitative measure due to the discontinuity of the thinner NiO layer and the porous nature of the underlying TiO_2 surface.

XRD measurements were performed for the identification of the crystalline structure of the TiO_2 and NiO/TiO_2 films (Figure 4.). The TiO_2 coatings were analysed after annealing in air for 2 h at 450 ºC, showing only anatase peaks at 2θ of 25.3° (101), 36.9º (103), 37.9° (004), 38,5º (112), 48.1° (200), 53.9° (105), 55.1° (211), 62,7º (204), 68.9º (116), 70.3° (220), 75,1º (215), 76º (301). All those peaks were identified with the JCPDS card 96-720-6076.

Regarding the NiO/TiO_2 coatings (Figure 4) no characteristic peaks related to NiO species were observed in the X-ray traces, most likely because the coatings were too thin. Additionally, it can be seen that the anatase TiO_2 structure did not measurably change with the addition of the NiO coatings.

The surface elemental composition and electronic state of the elements of the coatings were determined by X-ray photoelectron spectroscopy (XPS). The overall XPS spectra are presented in Figure 5a, showing the presence of Ti 2p, O 1s, C 1s and Ni 2p peaks. Carbon peaks can be explained by the presence of adventitious carbon on the surface. A high-resolution XPS spectrum for Ti 2p is shown in Figure 5b. Two main peaks can be attributed to Ti $2p_{1/2}$ and Ti $2p_{3/2}$, which are in good agreement with literature values for the Ti^{4+} valence state present in TiO_2 [52]. As can be observed, the intensity of the signal decreases for TiO_2-Ni due to the presence of a NiO coating. Through XPS, the formation of NiO instead of Ni was confirmed. As discussed earlier, the Ni was sputtered in metallic mode but instead of Ni metallic films, NiO films were obtained.

A high-resolution XPS spectrum for the Ni 2p region is shown in Figure 6. This spectrum can be divided into two parts: the first one on the left is composed of two peaks located at 879.4 eV and 872.8 eV, which can be attributed to the satellite peak and the Ni $2p_{1/2}$ peak, respectively. The second part of the spectra exhibits a satellite peak located at 860.5 eV and the Ni $2p_{3/2}$ peak located around 856 eV. Both of Ni 2p peaks can be deconvoluted in several peaks, confirming the presence of several oxidation states for Ni in the coating: Ni^{3+} (with peaks located at 874.5 eV and 855.5 eV), Ni^{2+} (with

peaks located at 873.8 eV and 854.2 eV) and N^0 (with peaks located at 872.3 and 852.6 eV). The latter one is composed of several peaks, showing different oxidation states for Ni. The peaks attributed to the presence of the Ni^{+3} oxidation state can be correlated to the high amount of oxygen adsorbed (531.2 eV), revealing the presence of NiOOH [53] on the surface of the sample. The peaks attributed to the presence of Ni^{+2} show the formation of the NiO layer. Finally, the presence of Ni^0 (552.6 eV) shows that some of the Ni on the coating remains metallic [54]. XPS spectra of O 1s are shown in Figure 7. For TiO_2 samples, the O 1s main peak can be deconvoluted in three individual peaks: two peaks at 533.2 eV and 531.7 eV that can be attributed to the presence of adsorbed oxygen species (such as O_2, H_2O, OH^-) [55,56]. And a third peak is attributed to the Ti-O bonds from the TiO_2 lattice. For NiO/TiO_2 samples, those 3 peaks can also be found, with the latter peak attributed to the Ni-O bonds from the NiO lattice. The valence-band (VB) spectra of TiO_2 and NiO/TiO_2 samples are shown in Figure 8. By extrapolating the valence band spectrum using linear fitting for each sample, the valence-band maximum (VBM) values were measured. For the TiO_2 sample, a VBM of 2.8 eV was measured. This value is similar to values that can be found in the literature [57]. When the NiO layer is deposited on top of

the TiO_2 coatings, the VBM measured shifts from 2.8 eV to 0.40 eV, which is in accordance with the formation of a p-type NiO layer [54].

In addition to the identification of the oxidation states of the elements, elemental quantification was performed on the samples. It must be noticed that a high concentration of C 1s was measured during the quantification, certainly due to impurities during the measurement (Tables S2 and S3).

The Raman spectra shown in Figure 9 matches the reported spectra of anatase found in the literature [58,59], with specific peaks located at 144, 397, 516, and 638 cm^{-1}. It can be also noted that the intensity of the peaks decreases with NiO layer thickness but changes are not observed in the anatase structure [57].

To determine the optical band gap, the transmittance of the TiO_2 and NiO/TiO_2 films was measured between 200 nm and 850 nm wavelength range. For the band gap estimation, assuming an indirect band gap, the absorption coefficient, α, was obtained using Equation 1, where t is the thickness of the film.

$$T \approx e^{-\alpha t} \quad (1)$$

Using the Tauc plot method [60], Eg was calculated using the absorption coefficient using Equation 2, by plotting $(\alpha h\nu)^{1/2}$ as a function of hν and extrapolating the linear region to the abscissa.

$$\alpha h\nu = C(h\nu - Eg)^{1/n} \quad (2)$$

where α is the absorbance coefficient, h is the Plank constant, ν is the frequency of vibration, Eg is the band gap energy and n is the value for TiO_2 indirect allowed transition, which is equal to 2 [61]. As can be seen in Figure 10, almost no change in terms of optical band gap can be observed when the NiO layer is deposited on the top of the TiO_2, which suggests that a p-n heterojunction is being formed.

3.2. Study of photocatalytic degradation of methylene blue

The degradation of methylene blue (MB) was studied for the coatings on glass substrates for 1 hour, with and without the NiO layer. Initially, the adsorption-desorption equilibrium of MB for the coatings was determined by keeping the samples immersed in a MB solution with constant stirring for 1 hour without illumination.

As shown in Figure 11a, using the natural logarithm of the relative absorbance ($Ln[A/A_0]$), plotted vs. time, a pseudo-first-order rate constant (k) is obtained for the reaction [5]. Figure 11b shows the degradation rate of methylene blue,

$A/A_{0,}$ with respect to time. All the experimental samples are compared to a commercial Pilkington Activ glass sample. Although this commercial product is produced using a different process, there is a lack of standards to compare to in this field and the Activ sample is acknowledged as providing a useful purpose in this case [62].

From these results, it can be concluded that TiO_2 presents photocatalytic activity under UV light with a k constant around $2x10^{-5}$ s^{-1} which agrees with literature reported values [49]. Also, the TiO_2 photocatalytic activity is improved with the addition of NiO coatings, with a more than 4 times improvement for the 10 nm NiO thick layer. Regarding degradation rates for the NiO/TiO_2 coatings, they also are in agreement with literature values reported, the slightly lower values can be attributed to differences in purity, structure or synthesis method [63,64]. This improvement in MB degradation for NiO/TiO_2 coatings could be due to the reduction of the recombination rate of TiO_2 h^+/e^- pairs by the presence of NiO and the improved electronic mobility caused by the formation of a p-n heterojunction, where the electrons produced in the conduction band of the p-type semiconductor (here NiO) are moved to the conduction band of the n-type semiconductor (here TiO_2). These photogenerated electrons are responsible for reducing adsorbed O_2 to $O_2^{-\cdot}$, which is considered a key step in MB oxidative decomposition. On the other

hand, the holes generated in the valence band of the n-type semiconductor are promoted to the valence band of the p-type semiconductor, reacting with absorbed H_2O or OH^-, which leads to the formation of strongly oxidative $OH^\cdot$ radicals. These radicals are thought to be the main driving force for photocatalytic oxidative reactions, reacting very fast with the MB adsorbed on the NiO surface [65–67]. The different p-n junctions created increase the charge separation efficiency of the material as confirmed by the lower band gap values achieved for pure TiO_2 by UV transmittance measurements. The formation of these radicals due to the formation of a p-n heterojunction is the main reason for the improvement of the charge carriers' separation and, consequently, photocatalytic efficiency [68,69]. As a future objective to complete this work, we intend to perform photoactivity measurements in the presence of scavengers [49,70].

Regarding the thickness of the NiO coatings, it appears that increasing thickness from 10 nm to 20 nm does not translate into a comparable improvement in photocatalytic activity. This could be because, despite the observed reduction of roughness in the 20 nm layer, which is equivalent to a reduction in surface area, the 20 nm NiO layer gives better coverage of the TiO_2 surface, improving the formation of new p-n heterojunctions. These two contradictory effects may be the reason why there is no remarkable increase

in photocatalytic activity when the thickness is increased. The influence of the thickness of NiO layers on photocatalytic activity is a subject that could be interesting to further analyse in future research. The degradation percentage and degradation rate constant of the coatings are summarized in Table 2.

Finally, stability measurements were performed with NiO/TiO_2 samples to confirm their photoactivity and stability over ten cycles. The obtained results are shown in Figure 12. From these measurements, several interesting conclusions can be drawn:

(i) A significant reduction between the degradation percentage of the 1^{st} cycle and the 2^{nd} cycle takes place, especially in the 10 nm NiO sample. The most probable reason for this reduction could be that when the 1^{st} measurement was carried out, the adsorption of the MB hadn't reached equilibrium and was still taking place while the samples were irradiated. This effect would probably be more noticeable in the 10 nm layer, due to its high porosity. For the rest of the cycles the degradation percentage is very stable when compared to the rest of the cycles, thus we can assume that no degradation of the coatings is taking place.

(ii) When the adsorption of the MB no longer takes place, the 20 nm NiO coating shows a slightly higher activity when compared with the 10 nm NiO coating.

(iii) Besides the 1st cycle, the coatings show high stability for the remainder of the measurements.

4. Conclusions

TiO_2 and NiO/TiO_2 coatings were prepared by DC and pulsed DC reactive magnetron sputtering and, after annealing, their photocatalytic activity was tested for methylene blue degradation. In this work, it was concluded that the incorporation of 10 nm and 20 nm NiO coatings on top of the TiO_2, modified the surface morphology without significantly changing the bandgap or crystalline structure of the coatings, but clearly resulted in a remarkable improvement of the MB degradation rate due to the formation of a p-n heterojunction that favoured charge carrier separation and electronic mobility. Although both NiO coatings improved the performance of the TiO_2 film, the thicker coating does not have a much bigger effect on activity probably due to the countering effect of reducing surface area and increasing p-n heterojunctions.

Acknowledgments

This research has received funding from the KMM-VIN Research Fellowship 2021 program, granted to Antía Villamayor (https://www.kmm-vin.eu/fellowships/).

Appendix A. Supplementary material

Supplementary material related to this article can be found in the online version.

References

[1] K. Niinimamp, G. Peters, H. Dahlbo, P. Perry, T. Rissanen, A. Gwilt, The environmental price of fast fashion, (n.d.). https://doi.org/10.1038/s43017-020-0039-9.

[2] T. Luttrell, S. Halpegamage, J. Tao, A. Kramer, E. Sutter, M. Batzill, Why is anatase a better photocatalyst than rutile? - Model studies on epitaxial TiO_2 films, Sci. Rep. 4 (2015) 1–8. https://doi.org/10.1038/srep04043.

[3] E. Pelizzetti, C. Minero, Mechanism of the photo-oxidative degradation of organic pollutants over TiO_2 particles, Electrochim. Acta. 38 (1993) 47–55. https://doi.org/10.1016/0013-4686(93)80009-O.

[4] J.M. Herrmann, J. Disdier, P. Pichat, S. Malato, J. Blanco, TiO_2-based solar photocatalytic detoxification of water containing organic pollutants. Case studies of 2,4-dichlorophenoxyaceticacid (2,4-D) and of benzofuran, Appl. Catal. B Environ. 17 (1998) 15–23. https://doi.org/10.1016/S0926-3373(97)00098-2.

[5] A. Houas, H. Lachheb, M. Ksibi, E. Elaloui, C. Guillard, J.M. Herrmann, Photocatalytic degradation pathway of methylene blue in water, Appl. Catal. B Environ. 31 (2001) 145–157. https://doi.org/10.1016/S0926-3373(00)00276-9.

[6] A. Naldoni, M. Altomare, G. Zoppellaro, N. Liu, Š. Kment, R. Zbořil, P. Schmuki, Photocatalysis with reduced TiO_2 : From Black TiO_2 to cocatalyst-free hydrogen production, ACS Catal. 9 (2019) 345–364. https://doi.org/10.1021/acscatal.8b04068.

[7] X. Kong, Z. Peng, R. Jiang, P. Jia, J. Feng, P. Yang, Q. Chi, W. Ye, F. Xu, P. Gao, Nanolayered Heterostructures of N-Doped TiO_2 and N-Doped Carbon for Hydrogen Evolution, ACS Appl. Nano Mater. 3 (2020) 1373–1381. https://doi.org/10.1021/ACSANM.9B02217/SUPPL_FILE/AN9B02217_SI_001.PDF.

[8] D. Jia, X. Li, Q. Chi, J. Low, P. Deng, W. Wu, Y. Wang, K. Zhu, W. Li, M. Xu, X. Xu, G. Jia, W. Ye, P. Gao, Y. Xiong, Direct Electron Transfer from Upconversion Graphene Quantum Dots to TiO_2 Enabling Infrared Light-Driven Overall Water Splitting, (2022). https://doi.org/10.34133/2022/9781453.

[9] A.E. Wiącek, A. Gozdecka, M. Jurak, Physicochemical Characteristics of Chitosan-TiO_2 Biomaterial. 1. Stability and Swelling Properties, Ind. Eng. Chem. Res. 57 (2018) 1859–1870. https://doi.org/10.1021/acs.iecr.7b04257.

[10] J.M. Janusz, J.A. Berson, Heterogeneous Photocatalytic Synthesis of Methane from Acetic Acid—New Kolbe Reaction Pathway, J. Am. Chem. Soc. 100 (1978) 2239–2240. https://doi.org/10.1021/JA00475A049/ASSET/JA00475A049.FP.PNG_V03.

[11] E. Santos, A.C. Catto, A.F. Peterline, W. Avansi, Transition metal (Nb and W) doped TiO_2 nanostructures: The role of metal doping in their photocatalytic activity and ozone gas-sensing performance, Appl. Surf. Sci. 579 (2022) 152146. https://doi.org/10.1016/J.APSUSC.2021.152146.

[12] N. Sriharan, T.S. Senthil, P. Soundarrajan, M. Kang, Surface modification

of TiO_2 nanorods with Mg doping for efficient photoelectrodes in dye sensitized solar cells, Appl. Surf. Sci. 585 (2022) 152719. https://doi.org/10.1016/J.APSUSC.2022.152719.

[13] T. Gao, T.-T. Li, X. Liao, J.-H. Lin, B.-C. Shiu, C.-W. Lou, Construction of Cu_2O/TiO_2 heterojunction photoelectrodes for photoelectrochemical determination of glucose, J. Mater. Res. Technol. 21 (2022) 798–809. https://doi.org/10.1016/J.JMRT.2022.09.043.

[14] F. Pinto, A. Wilson, B. Moss, A. Kafizas, Systematic Exploration of WO_3/TiO_2 Heterojunction Phase Space for Applications in Photoelectrochemical Water Splitting, J. Phys. Chem. C. 126 (2022) 871–884. https://doi.org/10.1021/ACS.JPCC.1C08403/ASSET/IMAGES/LARGE/JP1C08403_0009.JPEG.

[15] Q. Chi, G. Zhu, D. Jia, W. Ye, Y. Wang, J. Wang, T. Tao, F. Xu, G. Jia, W. Li, P. Gao, Built-in electric field for photocatalytic overall water splitting through a TiO_2/BiOBr P–N heterojunction, Nanoscale. 13 (2021) 4496–4504. https://doi.org/10.1039/D0NR08928A.

[16] H. Zhang, J. Cai, Y. Wang, M. Wu, M. Meng, Y. Tian, X. Li, J. Zhang, L. Zheng, Z. Jiang, J. Gong, Insights into the effects of surface/bulk defects on

photocatalytic hydrogen evolution over TiO_2 with exposed {001} facets, Appl. Catal. B Environ. 220 (2018) 126–136. https://doi.org/10.1016/J.APCATB.2017.08.046.

[17] S.A. Rawool, M.R. Pai, A.M. Banerjee, A. Arya, R.S. Ningthoujam, R. Tewari, R. Rao, B. Chalke, P. Ayyub, A.K. Tripathi, S.R. Bharadwaj, pn Heterojunctions in NiO:TiO_2 composites with type-II band alignment assisting sunlight driven photocatalytic H_2 generation, Appl. Catal. B Environ. 221 (2018) 443–458. https://doi.org/10.1016/J.APCATB.2017.09.004.

[18] L. Wen, B. Liu, X. Zhao, K. Nakata, T. Murakami, A. Fujishima, Synthesis, Characterization, and Photocatalysis of Fe-Doped TiO_2 : A Combined Experimental and Theoretical Study, Int. J. Photoenergy. 2012 (2012). https://doi.org/10.1155/2012/368750.

[19] H. Mourão, W. Junior, C.R.-M.C. and Physics, undefined 2012, Hydrothermal synthesis of Ti oxide nanostructures and TiO_2: SnO_2 heterostructures applied to the photodegradation of rhodamine B, Elsevier. (n.d.). https://www.sciencedirect.com/science/article/pii/S025405841200466X (accessed January 5, 2023).

[20] J. Wang, Z. Jiang, L. Zhang, P. Kang, Y. Xie, … Y.L.-U., undefined 2009, Sonocatalytic degradation of some dyestuffs and comparison of catalytic activities of nano-sized TiO_2, nano-sized ZnO and composite TiO_2/ZnO powders, Elsevier. (n.d.). https://www.sciencedirect.com/science/article/pii/S1350417708001326 (accessed January 5, 2023).

[21] Q. Zhu, N. Liu, N. Zhang, Y. Song, M.S. Stanislaus, C. Zhao, Y. Yang, Efficient photocatalytic removal of RhB, MO and MB dyes by optimized Ni/NiO/TiO_2 composite thin films under solar light irradiation, J. Environ. Chem. Eng. 6 (2018) 2724–2732. https://doi.org/10.1016/j.jece.2018.04.017.

[22] P. Brault, A. Caillard, A.L. Thomann, J. Mathias, C. Charles, R.W. Boswell, S. Escribano, J. Durand, T. Sauvage, Plasma sputtering deposition of platinum into porous fuel cell electrodes, J. Phys. D. Appl. Phys. 37 (2004) 3419–3423. https://doi.org/10.1088/0022-3727/37/24/010.

[23] W. Liu, S.C.-A.M. Research, undefined 2011, Visible-light activity evaluation of pn junction photocatalyst NiO/TiO_2 prepared by sol-gel method, Trans Tech Publ. (n.d.). https://www.scientific.net/AMR.152-153.441 (accessed January 5, 2023).

[24] Y. Chen, J. Crittenden, S.H.-… science & technology, undefined 2005, Preparation of a Novel TiO_2-Based p−n Junction Nanotube Photocatalyst, ACS Publ. 39 (2005) 1201–1208. https://doi.org/10.1021/es049252g.

[25] Y. Zheng, B. Zhu, H. Chen, W. You, C. Jiang, J. Yu, Hierarchical flower-like nickel(II) oxide microspheres with high adsorption capacity of Congo red in water, J. Colloid Interface Sci. 504 (2017) 688–696. https://doi.org/10.1016/J.JCIS.2017.06.014.

[26] F. Motahari, M.R. Mozdianfard, M. Salavati-Niasari, Synthesis and adsorption studies of NiO nanoparticles in the presence of H_2 acacen ligand, for removing Rhodamine B in wastewater treatment, Process Saf. Environ. Prot. 93 (2015) 282–292. https://doi.org/10.1016/J.PSEP.2014.06.006.

[27] T. Sreethawong, S. Ngamsinlapasathian, S. Yoshikawa, Surfactant-aided sol–gel synthesis of mesoporous-assembled TiO_2–NiO mixed oxide nanocrystals and their photocatalytic azo dye degradation activity, Chem. Eng. J. 192 (2012) 292–300. https://doi.org/10.1016/J.CEJ.2012.04.006.

[28] L. Chu, M. Li, P. Cui, Y. Jiang, Z. Wan, S. Dou, The Study of NiO/TiO_2 Photocatalytic Activity for Degradation of Methylene Orange, Energy Environ. Focus. 3 (2014) 371–374. https://doi.org/10.1166/EEF.2014.1125.

[29] C. Yu, M. Li, D. Yang, K. Pan, F. Yang, Y. Xu, L. Yuan, Y. Qu, W. Zhou, NiO nanoparticles dotted TiO_2 nanosheets assembled nanotubes P-N heterojunctions for efficient interface charge separation and photocatalytic hydrogen evolution, Appl. Surf. Sci. 568 (2021) 150981. https://doi.org/10.1016/J.APSUSC.2021.150981.

[30] J.H. Yu, H. Yang, R.H. Jung, J.W. Lee, J.H. Boo, Hierarchical NiO/TiO_2 composite structures for enhanced electrochromic durability, Thin Solid Films. 664 (2018) 1–5. https://doi.org/10.1016/J.TSF.2018.07.049.

[31] U.T. Nakate, R. Ahmad, P. Patil, Y.T. Yu, Y.B. Hahn, Ultra thin NiO nanosheets for high performance hydrogen gas sensor device, Appl. Surf. Sci. 506 (2020) 144971. https://doi.org/10.1016/J.APSUSC.2019.144971.

[32] I. Barton, V. Matejec, J. Matousek, Photocatalytic activity of nanostructured TiO_2 coating on glass slides and optical fibers for methylene blue or methyl orange decomposition under different light excitation, J. Photochem. Photobiol. A Chem. 317 (2016) 72–80. https://doi.org/10.1016/j.jphotochem.2015.11.009.

[33] A. Najafidoust, S. Allahyari, N. Rahemi, M. Tasbihi, Uniform coating of TiO_2 nanoparticles using biotemplates for photocatalytic wastewater treatment, Ceram. Int. 46 (2020) 4707–4719.

https://doi.org/10.1016/j.ceramint.2019.10.202.

[34] M. Yamagishi, S. Kuriki, P.K. Song, Y. Shigesato, Thin film TiO_2 photocatalyst deposited by reactive magnetron sputtering, Thin Solid Films. 442 (2003) 227–231. https://doi.org/10.1016/S0040-6090(03)00987-8.

[35] J. Singh, S.A. Khan, J. Shah, R.K. Kotnala, S. Mohapatra, Nanostructured TiO_2 thin films prepared by RF magnetron sputtering for photocatalytic applications, Appl. Surf. Sci. 422 (2017) 953–961. https://doi.org/10.1016/J.APSUSC.2017.06.068.

[36] G. Žerjav, G. Scandura, C. Garlisi, G. Palmisano, A. Pintar, Sputtered vs. sol-gel TiO_2-doped films: Characterization and assessment of aqueous bisphenol A oxidation under UV and visible light radiation, Catal. Today. 357 (2020) 380–391. https://doi.org/10.1016/J.CATTOD.2019.09.027.

[37] B. Hao, J. Guo, L. Zhang, H. Ma, Cr-doped TiO_2/CuO photocatalytic nanofilms prepared by magnetron sputtering for wastewater treatment, Ceram. Int. 48 (2022) 7106–7116. https://doi.org/10.1016/J.CERAMINT.2021.11.270.

[38] K.R. Reyes-Gil, D.B. Robinson, WO_3-enhanced TiO_2 Nanotube Photoanodes for Solar Water Splitting with Simultaneous Wastewater Treatment, ACS Appl. Mater. Interfaces. 5 (2013) 12400–12410.

https://doi.org/10.1021/AM403369P/SUPPL_FILE/AM403369P_SI_001.PDF.

[39] M. Ratova, R. Klaysri, P. Praserthdam, P.J. Kelly, Pulsed DC magnetron sputtering deposition of crystalline photocatalytic titania coatings at elevated process pressures, Mater. Sci. Semicond. Process. 71 (2017) 188–196. https://doi.org/10.1016/j.mssp.2017.07.028.

[40] S. Takeda, S. Suzuki, H. Odaka, H. Hosono, Photocatalytic TiO_2 thin film deposited onto glass by DC magnetron sputtering, Thin Solid Films. 392 (2001) 338–344. https://doi.org/10.1016/S0040-6090(01)01054-9.

[41] P. Pansila, N. Witit-Anun, S. Chaiyakun, Influence of sputtering power on structure and photocatalyst properties of DC magnetron sputtered TiO_2 thin film, Procedia Eng. 32 (2012) 862–867. https://doi.org/10.1016/j.proeng.2012.02.024.

[42] L. Zhang, J. Guo, B. Hao, H. Ma, WO_3/TiO_2 heterojunction photocatalyst prepared by reactive magnetron sputtering for Rhodamine B dye degradation, Opt. Mater. (Amst). 133 (2022) 113035. https://doi.org/10.1016/J.OPTMAT.2022.113035.

[43] B. Hao, J. Guo, L. Zhang, H. Ma, Magnetron sputtered TiO_2/CuO heterojunction thin films for efficient photocatalysis of Rhodamine B, J.

Alloys Compd. 903 (2022) 163851. https://doi.org/10.1016/J.JALLCOM.2022.163851.

[44] D. Ramírez-Ortega, D. Guerrero-Araque, P. Acevedo-Peña, E. Reguera, H.A. Calderon, R. Zanella, Enhancing the photocatalytic hydrogen production of the ZnO–TiO_2 heterojunction by supporting nanoscale Au islands, Int. J. Hydrogen Energy. 46 (2021) 34333–34343. https://doi.org/10.1016/J.IJHYDENE.2021.08.019.

[45] T.T. Nguyen, M. Patel, S. Kim, R.A. Mir, J. Yi, V.A. Dao, J. Kim, Transparent photovoltaic cells and self-powered photodetectors by TiO_2/NiO heterojunction, J. Power Sources. 481 (2021) 228865. https://doi.org/10.1016/J.JPOWSOUR.2020.228865.

[46] Y. Tian, B. Chang, G. Wang, L. Li, L. Gong, B. Wang, R. Yuan, W. Zhou, Magnetron sputtering tuned "π back-donation" sites over metal oxides for enhanced electrocatalytic nitrogen reduction, J. Mater. Chem. A. 10 (2022) 2800–2806. https://doi.org/10.1039/D1TA10273G.

[47] H. Tomaszewski, H. Poelman, D. Depla, D. Poelman, R. De Gryse, L. Fiermans, M.F. Reyniers, G. Heynderickx, G.B. Marin, TiO_2 films prepared by DC magnetron sputtering from ceramic targets, Vacuum. 68 (2002) 31–38. https://doi.org/10.1016/S0042-207X(02)00279-8.

[48] S. Schiller, U. Heisig, K. Steinfelder, J. Strümpfel, Reactive D.C. sputtering with the magnetron-plasmatron for tantalum pentoxide and titanium dioxide films, Thin Solid Films. 63 (1979) 369–375. https://doi.org/10.1016/0040-6090(79)90042-7.

[49] M. Grao, M. Ratova, C.C. Amorim, R.B.P. Marcelino, P. Kelly, Crystalline TiO_2 supported on stainless steel mesh deposited in a one step process via pulsed DC magnetron sputtering for wastewater treatment applications, J. Mater. Res. Technol. 9 (2020) 5761–5773. https://doi.org/10.1016/j.jmrt.2020.03.101.

[50] M. Grao, J. Redfern, P.J. Kelly, M. Ratova, Magnetron co-sputtered $Bi_{12}TiO_{20}/Bi_4Ti_3O_{12}$ composite – An efficient photocatalytic material with photoinduced oxygen vacancies for water treatment application, Appl. Surf. Sci. 552 (2021) 149486. https://doi.org/10.1016/J.APSUSC.2021.149486.

[51] J.A. Thornton, Influence of apparatus geometry and deposition conditions on the structure and topography of thick sputtered coatings, Undefined. 11 (1974) 666–670. https://doi.org/10.1116/1.1312732.

[52] P. Stefanov, M. Shipochka, P. Stefchev, Z. Raicheva, V. Lazarova, L. Spassov, XPS characterization of TiO_2 layers deposited on quartz plates, J. Phys. Conf. Ser. 100 (2008). https://doi.org/10.1088/1742-

6596/100/1/012039.

[53] M.C. Biesinger, B.P. Payne, L.W.M. Lau, A. Gerson, R.S.C. Smart, X-ray photoelectron spectroscopic chemical state quantification of mixed nickel metal, oxide and hydroxide systems, Surf. Interface Anal. 41 (2009) 324–332. https://doi.org/10.1002/SIA.3026.

[54] R. Karsthof, H. von Wenckstern, J. Zúñiga-Pérez, C. Deparis, M. Grundmann, Nickel Oxide–Based Heterostructures with Large Band Offsets, Phys. Status Solidi Basic Res. 257 (2020). https://doi.org/10.1002/PSSB.201900639.

[55] B. Zhou, X. Jiang, Z. Liu, R. Shen, A. V. Rogachev, Preparation and characterization of TiO_2 thin film by thermal oxidation of sputtered Ti film, Undefined. 16 (2013) 513–519. https://doi.org/10.1016/J.MSSP.2012.05.001.

[56] B. Bharti, S. Kumar, H.-N. Lee, R. Kumar, Formation of oxygen vacancies and Ti^{3+} state in TiO_2 thin film and enhanced optical properties by air plasma treatment OPEN, Nat. Publ. Gr. (2016). https://doi.org/10.1038/srep32355.

[57] Z.H. Ibupoto, M.A. Abbasi, X. Liu, M.S. Alsalhi, M. Willander, The Synthesis of NiO/TiO_2 Heterostructures and Their Valence Band Offset

Determination, (2014). https://doi.org/10.1155/2014/928658.

[58] O. Frank, M. Zukalova, B. Laskova, J. Kürti, J. Koltai, L. Kavan, Raman spectra of titanium dioxide (anatase, rutile) with identified oxygen isotopes (16, 17, 18), Phys. Chem. Chem. Phys. 14 (2012) 14567–14572. https://doi.org/10.1039/C2CP42763J.

[59] S. Challagulla, K. Tarafder, R. Ganesan, S. Roy, Structure sensitive photocatalytic reduction of nitroarenes over TiO_2, Sci. Rep. 7 (2017). https://doi.org/10.1038/S41598-017-08599-2.

[60] J. Tauc, R. Grigorovici, A. Vancu, Optical Properties and Electronic Structure of Amorphous Germanium, Phys. Status Solidi. 15 (1966) 627–637. https://doi.org/10.1002/PSSB.19660150224.

[61] R.B.P. Marcelino, C.C. Amorim, M. Ratova, B. Delfour-Peyrethon, P. Kelly, Novel and versatile TiO_2 thin films on PET for photocatalytic removal of contaminants of emerging concern from water, Chem. Eng. J. 370 (2019) 1251–1261. https://doi.org/10.1016/J.CEJ.2019.03.284.

[62] M. Ratova, P.J. Kelly, G.T. West, X. Xia, Y. Gao, materials Deposition of Visible Light Active Photocatalytic Bismuth Molybdate Thin Films by Reactive Magnetron Sputtering, (n.d.). https://doi.org/10.3390/ma9020067.

[63] Z. Wu, Y. Wang, L. Sun, Y. Mao, M. Wang, C. Lin, An ultrasound-assisted

deposition of NiO nanoparticles on TiO_2 nanotube arrays for enhanced photocatalytic activity, J. Mater. Chem. A. 2 (2014) 8223–8229. https://doi.org/10.1039/C4TA00850B.

[64] J.Z. Chen, T.H. Chen, L.W. Lai, P.Y. Li, H.W. Liu, Y.Y. Hong, D.S. Liu, Preparation and Characterization of Surface Photocatalytic Activity with NiO/TiO_2 Nanocomposite Structure, Mater. 2015, Vol. 8, Pages 4273-4286. 8 (2015) 4273–4286. https://doi.org/10.3390/MA8074273.

[65] X. Wan, M. Yuan, S.L. Tie, S. Lan, Effects of catalyst characters on the photocatalytic activity and process of NiO nanoparticles in the degradation of methylene blue, Appl. Surf. Sci. 277 (2013) 40–46. https://doi.org/10.1016/J.APSUSC.2013.03.126.

[66] R. Zuo, G. Du, W. Zhang, L. Liu, Y. Liu, L. Mei, Z. Li, Photocatalytic degradation of methylene blue using TiO_2 impregnated diatomite, Adv. Mater. Sci. Eng. 2014 (2014). https://doi.org/10.1155/2014/170148.

[67] M. Shaban, A.M. Ahmed, N. Shehata, M.A. Betiha, A.M. Rabie, Ni-doped and Ni/Cr co-doped TiO_2 nanotubes for enhancement of photocatalytic degradation of methylene blue, J. Colloid Interface Sci. 555 (2019) 31–41. https://doi.org/10.1016/J.JCIS.2019.07.070.

[68] M. Faisal, F.A. Harraz, A.A. Ismail, A.M. El-Toni, S.A. Al-Sayari, A. Al-

Hajry, M.S. Al-Assiri, Novel mesoporous NiO/TiO_2 nanocomposites with enhanced photocatalytic activity under visible light illumination, Ceram. Int. 44 (2018) 7047–7056. https://doi.org/10.1016/J.CERAMINT.2018.01.140.

[69] J. Yu, W. Wang, B. Cheng, Synthesis and Enhanced Photocatalytic Activity of a Hierarchical Porous Flowerlike p–n Junction NiO/TiO_2 Photocatalyst, Chem. – An Asian J. 5 (2010) 2499–2506. https://doi.org/10.1002/ASIA.201000550.

[70] I. Khan, K. Saeed, I. Zekker, B. Zhang, A.H. Hendi, A. Ahmad, S. Ahmad, N. Zada, H. Ahmad, L.A. Shah, T. Shah, I. Khan, Review on Methylene Blue: Its Properties, Uses, Toxicity and Photodegradation, Water 2022, Vol. 14, Page 242. 14 (2022) 242. https://doi.org/10.3390/W14020242.

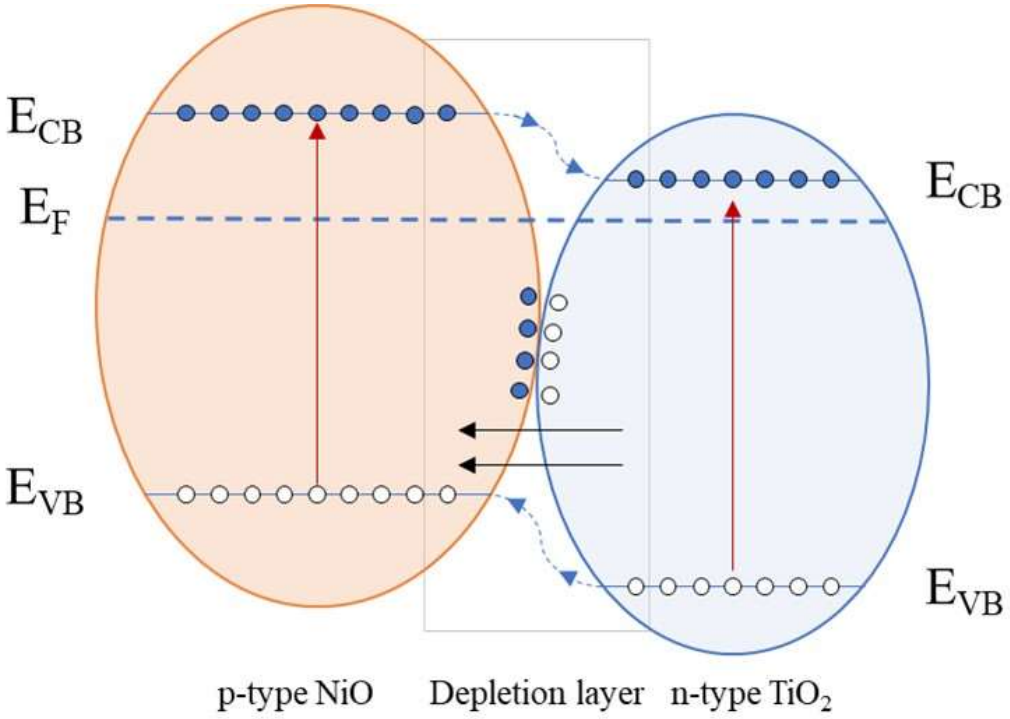

Figure 1. Scheme of a NiO/TiO_2 p-n heterojunction

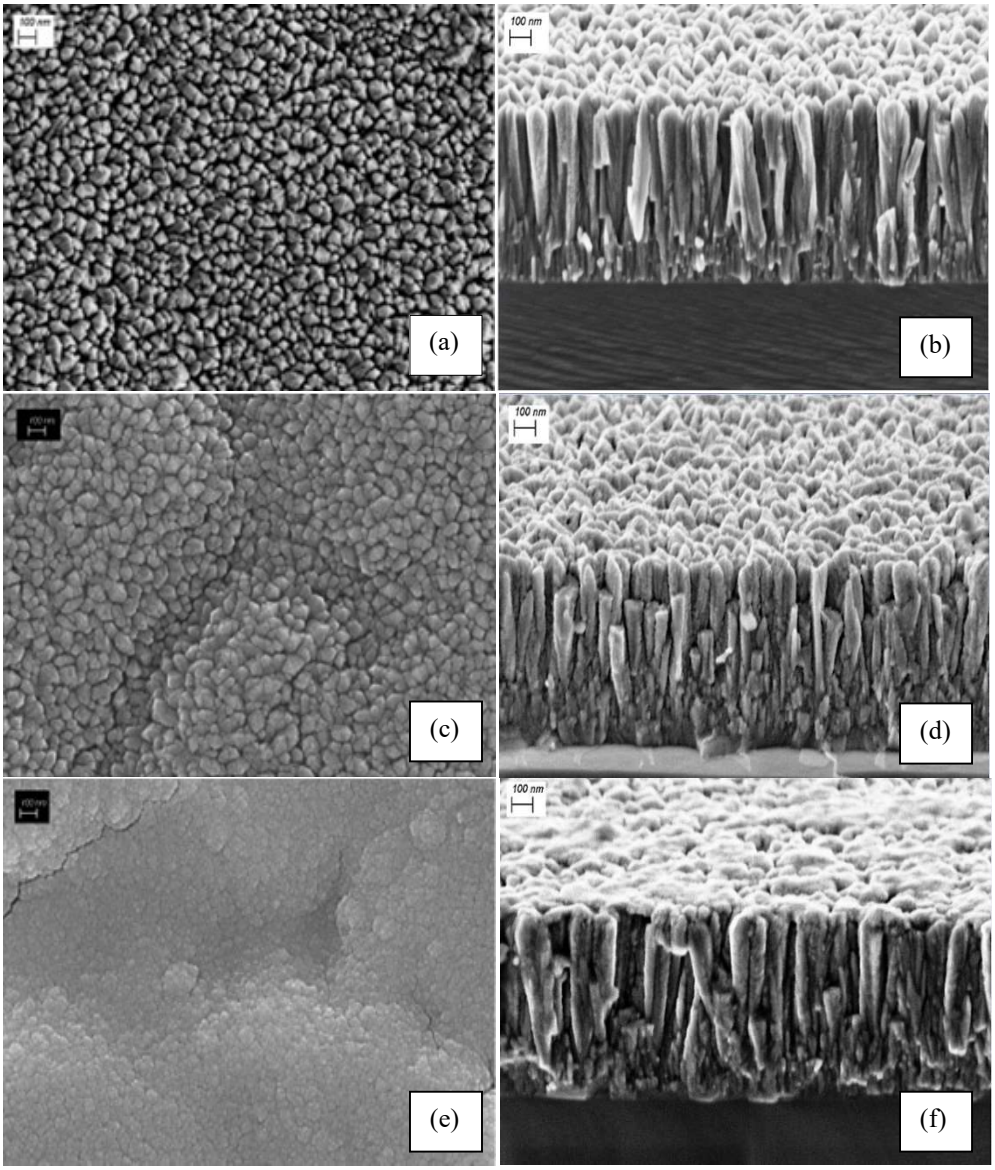

Figure 2. SEM images of (a, b) TiO_2 (c, d) 10 nm NiO/TiO_2 and (e, f) 20 nm NiO/TiO_2 coatings over a silicon substrate.

(a)

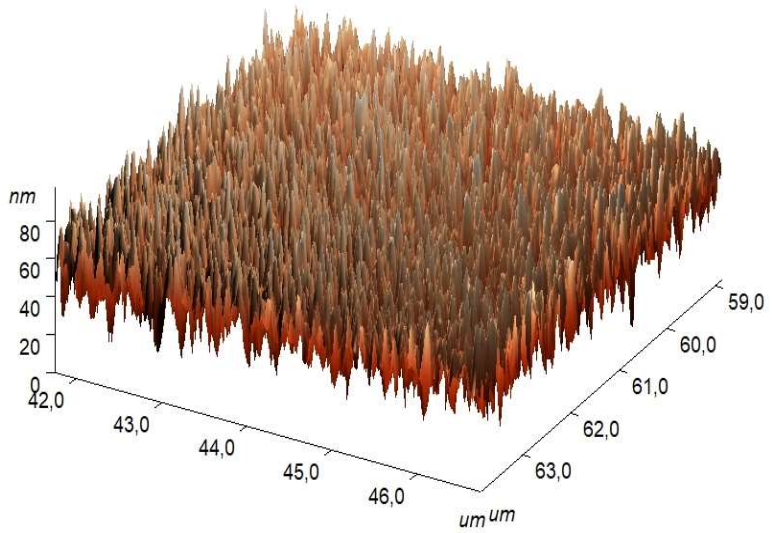

(b)

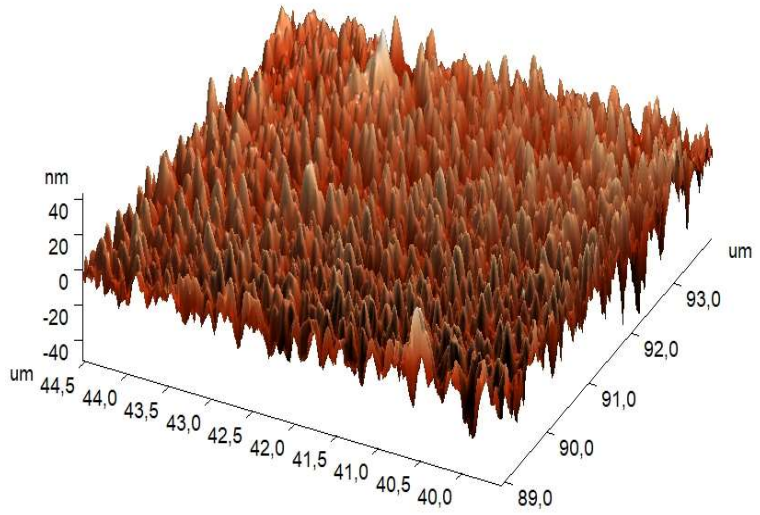

Figure 3. 3D-AFM images of (a) 10 nm NiO/TiO_2 and (b) 20 nm NiO/TiO_2 coatings.

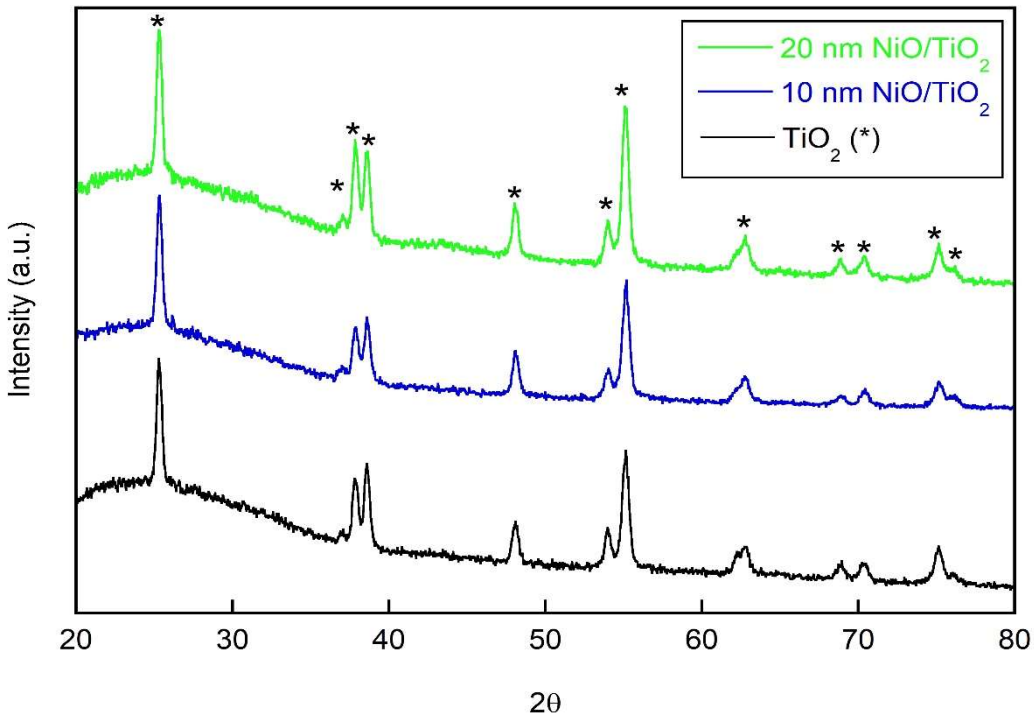

Figure 4. XRD spectra of anatase TiO_2 and NiO/TiO_2 coatings

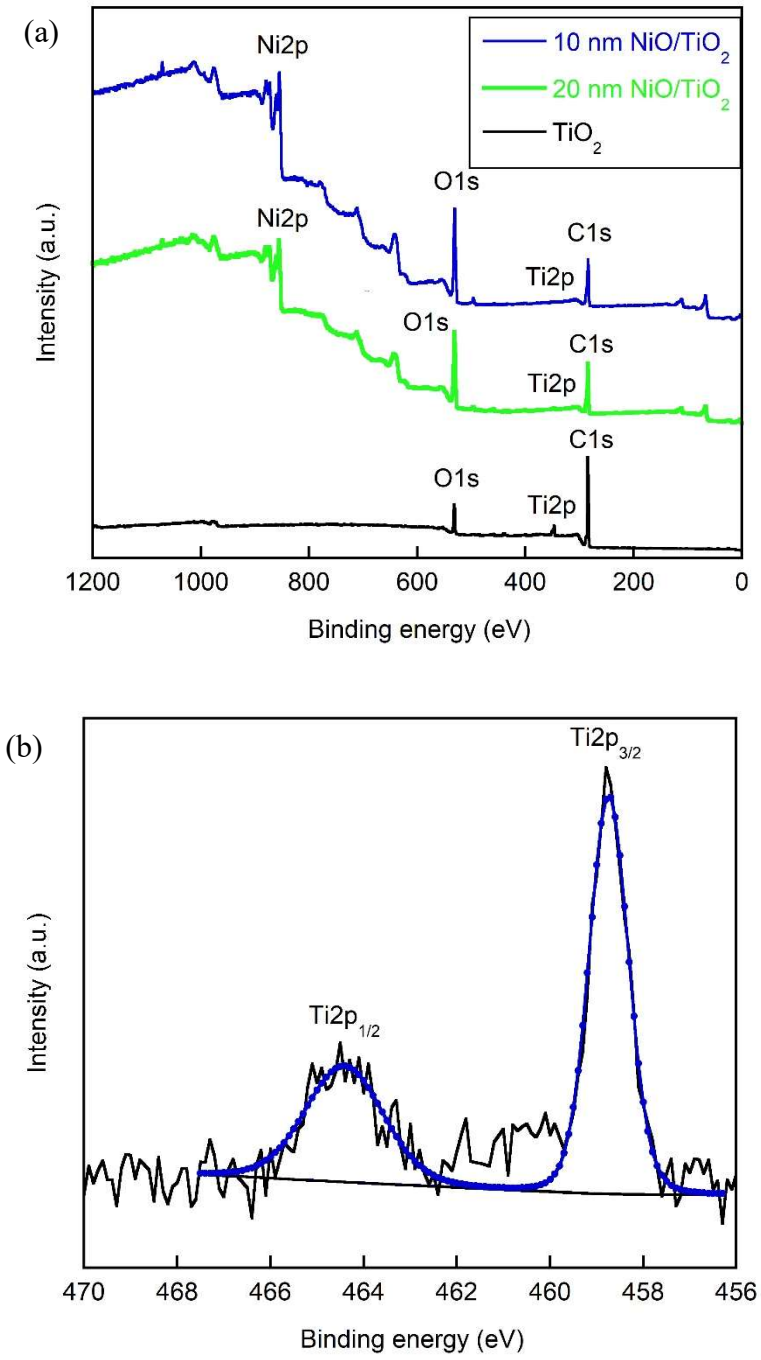

Figure 5. XPS spectra of (a) all samples and (b)Ti 2p peaks for TiO_2.

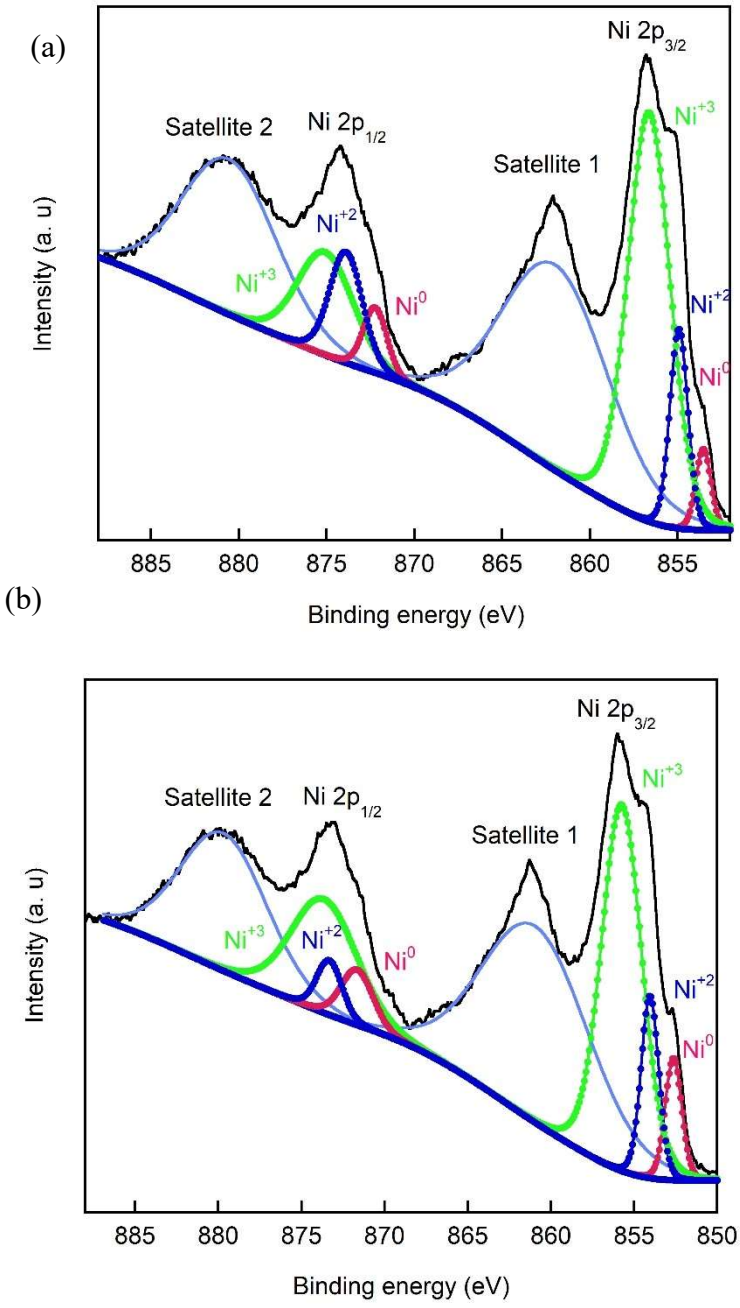

Figure 6. XPS spectra of Ni 2p for NiO/TiO_2 coatings of (a) 10 nm and (b) 20 nm.

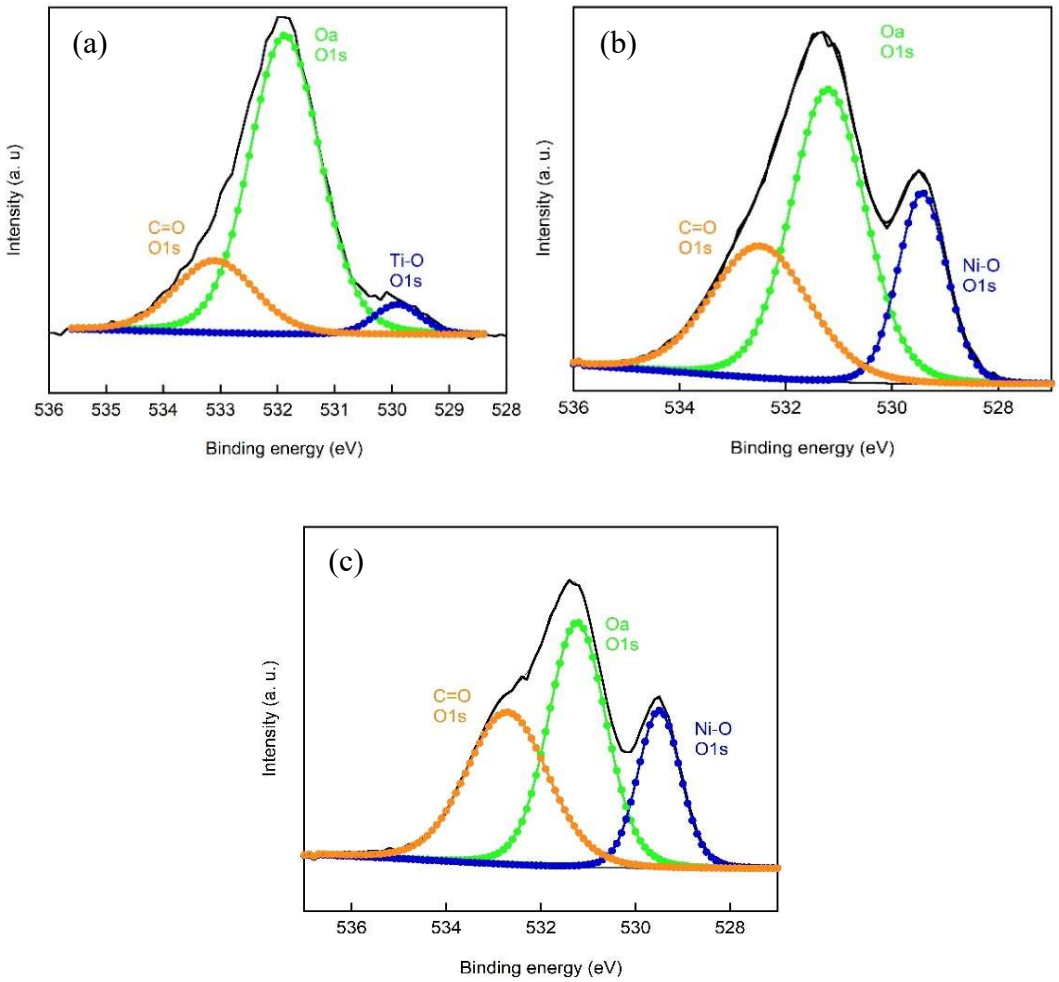

Figure 7. XPS spectra of O1s for (a) TiO_2 and (b) 10 nm and (c) 20 nm NiO/TiO_2 coatings.

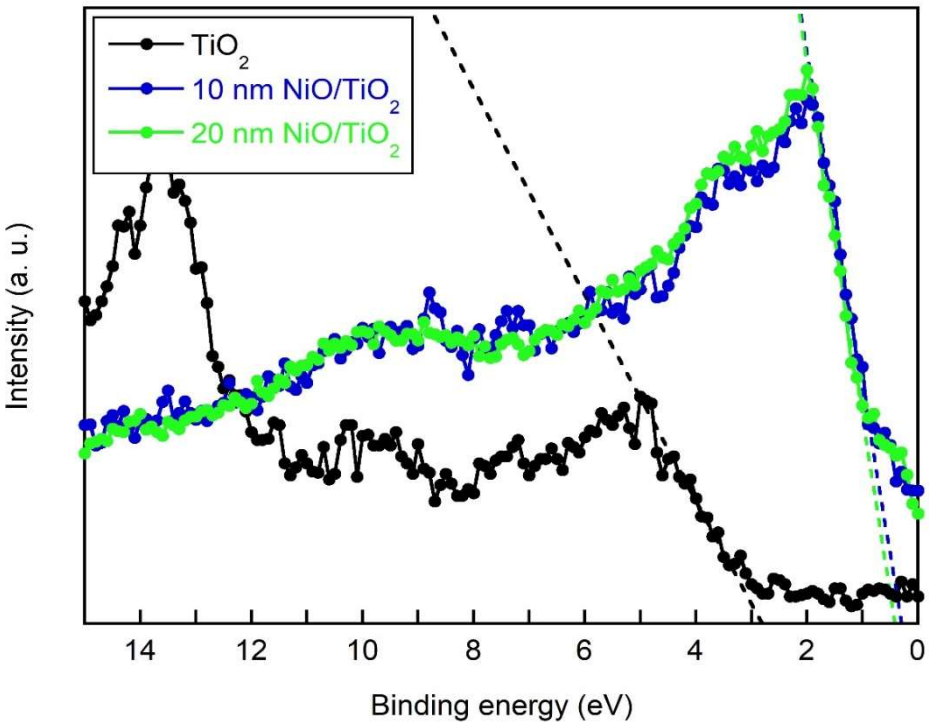

Figure 8. VB spectra of all samples for VBM determination.

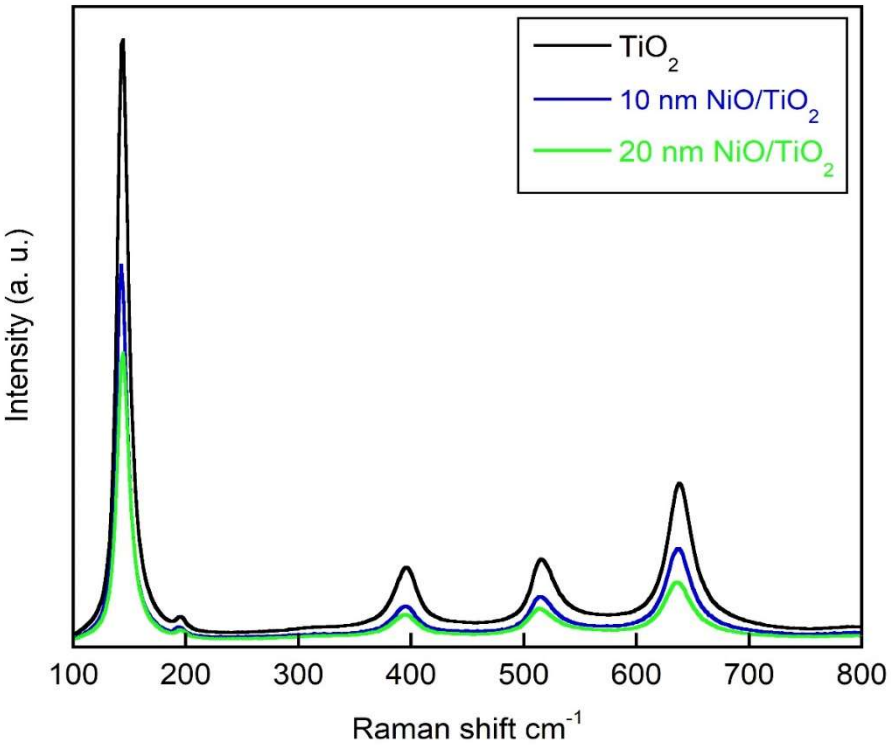

Figure 9. Raman spectra of all samples.

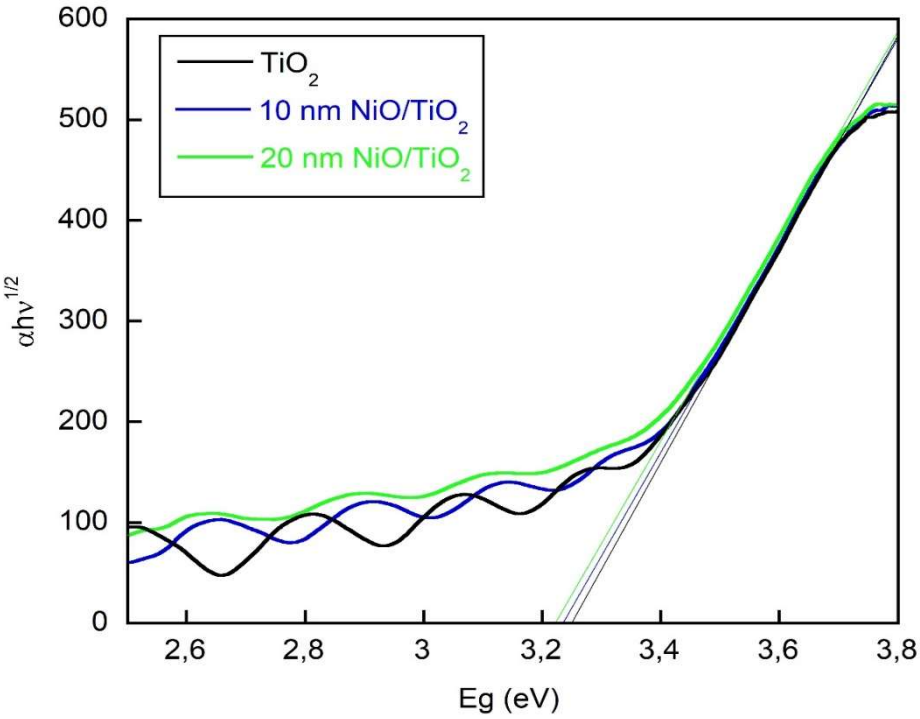

Figure 10. Optical bandgap of all samples.

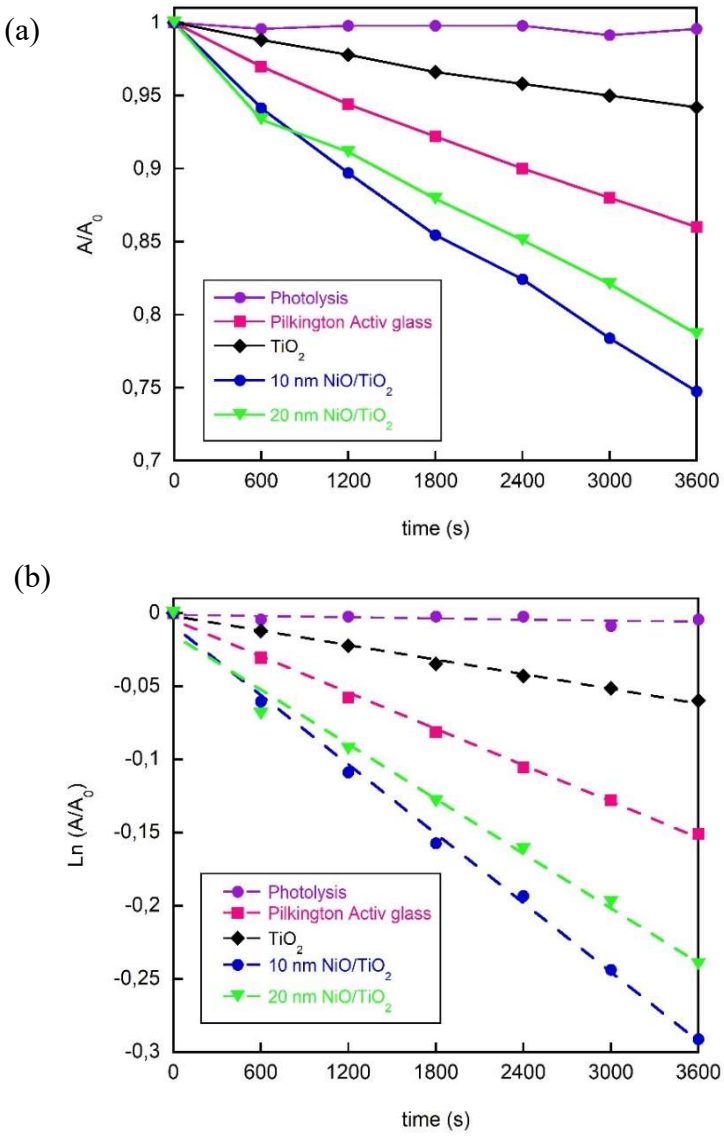

Figure 11. (a) The degradation rate of MB for the photocatalytic coatings and (b) determination of rate constants for MB degradation reaction using a first-order kinetic model under UV light.

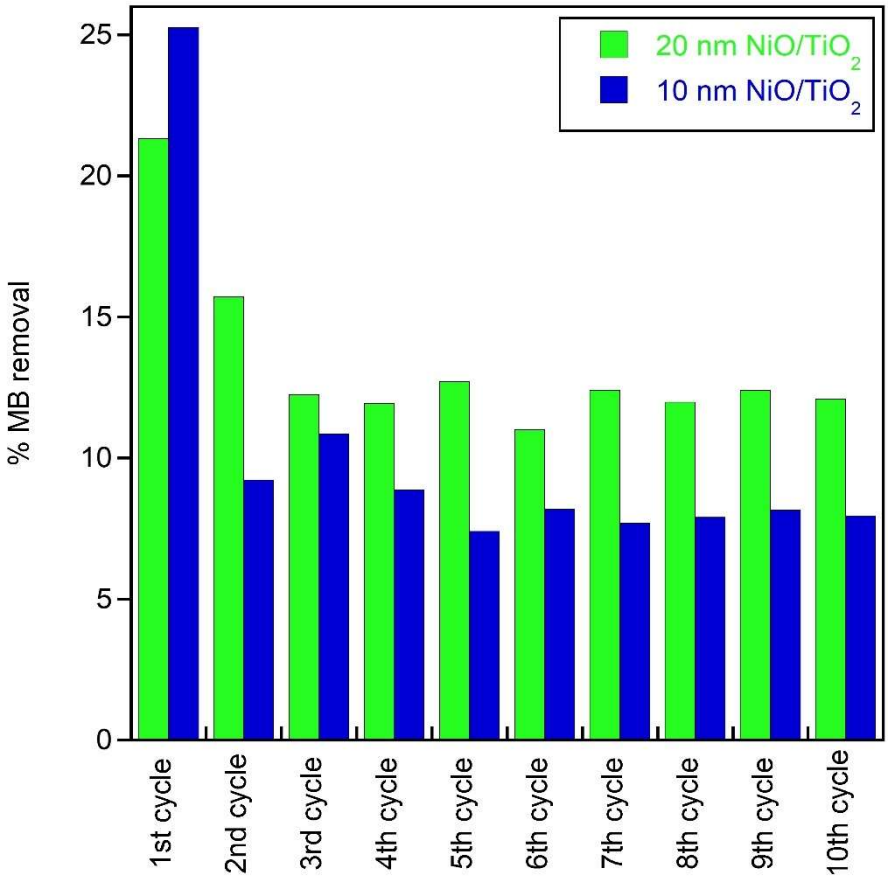

Figure 12. Stability test of NiO/TiO_2 samples for MB degradation .

Table 2. Degradation percentage and degradation rate constant under UV for 1h.

Sample	R (%)	k (s^{-1})
Pilkington	14	$4.31x10^{-5}$
TiO_2	5.8	$1.73x10^{-5}$
10 nm NiO/TiO_2	25.3	$8.22x10^{-5}$
20 nm NiO/TiO_2	21.3	$6.79x10^{-5}$